

See discussions, stats, and author profiles for this publication at: <https://www.researchgate.net/publication/230635962>

Quantum nonadiabatic dynamics of hydrogen exchange reactions

ARTICLE · NOVEMBER 2009

READS

78

3 AUTHORS, INCLUDING:



B. Jayachander Rao

University of Coimbra

12 PUBLICATIONS 51 CITATIONS

SEE PROFILE



Susanta Mahapatra

University of Hyderabad

114 PUBLICATIONS 1,636 CITATIONS

SEE PROFILE



Quantum nonadiabatic dynamics of hydrogen exchange reactions

T. Rajagopala Rao, B. Jayachander Rao, S. Mahapatra *

School of Chemistry, University of Hyderabad, Hyderabad 500 046, India

ARTICLE INFO

Article history:

Received 8 August 2009

Accepted 7 October 2009

Available online 13 October 2009

Keywords:

Nonadiabatic quantum dynamics

Integral reaction cross section

Reaction probability

Thermal rate constant

ABSTRACT

In continuation of our earlier effort to understand the nonadiabatic coupling effects in the prototypical $\text{H} + \text{H}_2$ exchange reaction [Jayachander Rao et al. Chem. Phys. 333 (2007) 135], we present here further quantum dynamical investigations on its isotopic variants. The present work also corrects a technical scaling error occurred in our previous studies on the $\text{H} + \text{HD}$ reaction. Initial state-selected total reaction cross sections and Boltzmann averaged thermal rate constants are calculated with the aid of a time-dependent wave packet approach employing the double many body expansion potential energy surfaces of the system. The theoretical results are compared with the experimental and other theoretical data whenever available. The results re-establish our earlier conclusion, on a more general perspective, that the electronic nonadiabatic effects are negligible on the important quantum dynamical observables of these reactive systems reported here.

© 2009 Elsevier B.V. All rights reserved.

1. Introduction

Investigation of electronic nonadiabatic effects in chemical reaction dynamics has become a topic of immense current interest. In this context, the $\text{H} + \text{H}_2$ exchange reaction has been a benchmark prototype for the theoretical studies, as it allows accurate quantum mechanical calculations to be performed because of its seemingly simple quantum chemistry. Its dynamical outcomes however, have been outstandingly difficult to understand [1].

The ($E \otimes e$)-Jahn–Teller (JT) effect [2] in the orbitally degenerate electronic ground states of H_3 leads to the occurrence of conical intersections (CIs) of its potential energy surfaces (PESs) at the D_{3h} equilateral triangular geometry [3,4]. The $\text{H} + \text{H}_2$ exchange reaction takes place on the repulsive lower adiabatic sheet of this JT split electronic ground state of H_3 . Investigation of the role of the bound (in absence of the JT coupling) upper adiabatic JT sheet on this reaction systems has attracted much attention in the research in contemporary chemical dynamics [5,6]. The JT coupling has been discovered to be very strong in H_3 , which leads to perhaps (known ever!) fastest nonradiative relaxation of the upper adiabatic sheet of the JT split PESs within a time scale of $\sim 3\text{--}6$ fs only [7,8]. On the other hand, the JT coupling apparently does not have such profound effects on the reactivity of the $\text{H} + \text{H}_2$ exchange reaction [5]. This surprising result is not clearly understood and remains to be an open issue till date.

It is well-known that the CIs of PESs are natural consequences of the JT instability of symmetric nonlinear molecular systems [3].

Electronic nonadiabatic effects prevail due to these intersections, ensuing a break-down of the adiabatic Born–Oppenheimer (BO) approximation [9]. Nuclei undergo electronic transitions during their dynamical evolution. One of the consequences of electronic nonadiabatic effects extensively exercised in the literature, is to rectify the multi-valuedness of the adiabatic electronic wave function when it encircles the CIs, a topological phenomenon, known as the geometric phase (GP) effects [10]. This topological correction, understandably is a part of the explicit surface coupling effect (consisting of the singular derivative and the non-BO coupling terms) of the nonadiabatic coupling operator. The effect of CIs on the reactive scattering dynamics of the $\text{H} + \text{H}_2$ and its isotopic variants are well studied in the literature in terms of the GP change of the adiabatic electronic wavefunction when encircling the CIs in a closed path in the nuclear coordinate space [11]. In order to account for the phase change and to make the total wavefunction single valued, a vector potential term is introduced into the nuclear Hamiltonian [12]. Early work on the GP effect in hydrogen exchange reaction was carried out by Mead [13]. This was followed by the pioneering calculations by Kuppermann and coworkers by using multivalued basis functions to include the GP [11]. The latter authors predicted strong GP effects in both the integral and differential reaction cross sections (DCSs). These findings stimulated further theoretical work by Kendrick [14], who performed time-independent calculations including the GP using the Mead–Truhlar vector potential formulation [12]. The GP effects were found to be small and appear in the state-to-state reaction probabilities only for the total energies higher than 1.8 eV above the H_3 potential minimum [14]. These effects which appear in the state-to-state reaction probabilities, cancel on summing over all partial wave contributions in the state-to-state integral cross sections (ICSSs).

* Corresponding author. Fax: +91 40 23011537/23012460.

E-mail addresses: smc@uohyd.ernet.in, susanta_m2004@yahoo.com (S. Mahapatra).

Subsequently, Juanes-Marcos et al. confirmed Kendrick's results [14] and extended them to higher impact parameters using an entirely different theoretical approach [15]. Furthermore, these authors were able to explain these observations using a topological argument [16] by demonstrating that the nuclear wavefunction splits into two components which interfere to cancel the GP effects in the ICSs and DCSs. But all the above calculations were carried out within the realm of the BO approximation, which include the GP effects either through multivalued basis functions [11] or through the vector potential method [14,15]. These calculations do not take an explicit account of the effects of the upper adiabatic PES on the dynamics.

Therefore, in order to account for the complete effects of the coupling of the upper surface on the dynamics, Mahapatra et al. developed a theoretical model to study the $H + H_2$ reaction dynamics on its conically intersecting ground electronic PES for the total angular momentum, $J = 0$ for the first time [5]. This study includes the GP effects along with other nonadiabatic coupling terms [5]. In this work, the authors have computed the initial state-selected and energy resolved reaction probabilities for the total angular momentum, $J = 0$, by considering both the lower and upper adiabatic sheets and the coupling between them for energies extending up to the three-body dissociation limit (~ 4.74 eV) of H_3 . The calculated reaction probabilities were found to reveal minor impact of nonadiabatic coupling on the reaction dynamics for $J = 0$ above the energetic minimum of the seam of CIs (~ 2.74 eV). In a subsequent study, Jayachander Rao et al. [17] have reported the initial state-selected integral reaction cross sections and thermal rate constants of $H + H_2$ (HD) reactions within the coupled states (CS) approximation [18]. This extended the earlier work of Mahapatra et al. [5] to the nonzero total angular momentum J . The nonadiabatic effects on the total reaction cross sections were found to be small in this study [17]. But the nonadiabatic effects were found to be quite substantial in the channel specific reaction probabilities of the $H + HD$ reaction [17]. The effect, however, gets canceled in the integral reaction cross sections. Recently, we found a mass scaling error occurred in the channel specific reaction probabilities of the $H + HD$ reaction shown in Ref. [17]. This technical error has been corrected and the correct results are given in this paper. Coupled and uncoupled surface studies were also performed by Ghosal et al. [19] for the $D + H_2$ reaction. Subsequently, Jayachander Rao et al. reported the effect of reagent rotation and vibration on the nonadiabatic quantum wave packet (WP) dynamics of $H + H_2$ reaction [20]. It was found that the rotational excitation of the reagent H_2 enhances the nonadiabatic effects whereas, the reagent vibrational excitation has only minor influence on the same [20]. The effect of Coriolis coupling (CC) terms on the dynamics of hydrogen exchange is being investigated in our group and a preliminary account of the same has been reported recently [21]. Recently, Althorpe and coworkers have studied the state-to-state reaction probabilities and cross sections for the $H + H_2$ reaction, at total energies up to 4.5 eV [6]. In this work, they have employed the diabatic theoretical model of Mahapatra et al. [5] to explicitly include all nonadiabatic surface coupling elements in the reaction dynamics of the $H + H_2$ reaction. The results of these calculations also show a very small contribution of upper electronic state to the state-to-state dynamics, even at energies much higher than the minimum of the seam of the CIs (~ 2.74 eV) [6].

In this paper the initial state-selected and energy resolved reaction probabilities, integral reaction cross sections and thermal rate constants are calculated for the $H + D_2$ (HD) and $D + H_2$ (HD) reactions within the CS approximation [18]. The reaction probabilities are reported up to the total energy of ~ 4.7 eV both with and without the surface coupling. All partial wave contributions up to the total angular momentum $J = 50$ are considered to calculate the converged integral reaction cross sections. Analysis of the reaction

probabilities, integral reaction cross sections show that the nonadiabatic effects are insignificant. The thermal rate constants calculated from the integral reaction cross sections compare well with the available theoretical and experimental results [22–29].

2. Theoretical details

The theoretical formalism employed to calculate the initial state-selected and energy resolved reaction probabilities, integral reaction cross sections and thermal rate constants for the $H + D_2$ (HD) and $D + H_2$ (HD) reactions is briefly outlined in this section. The reaction probabilities are calculated from the expectation values of the quantum flux operator in the basis of the energy normalized time-independent reactive scattering wavefunction. The initial WP, $|\Psi(t=0)\rangle$, pertinent to the reagents is prepared in the asymptotic reagent channel and then propagated on the coupled manifold of the electronic ground state of the system with the aid of the time-dependent Schrödinger equation (TDSE). For an explicitly time-independent Hamiltonian (like in the present case), the solution of TDSE reads

$$|\Psi(t)\rangle = \exp\left[\frac{-i\hat{H}t}{\hbar}\right]|\Psi(t=0)\rangle, \quad (1)$$

where, $|\Psi(t)\rangle$ is the wavefunction of the reacting system at time t , and \hat{H} defines the Hamiltonian operator of the collisional system.

The interaction Hamiltonian of the ground electronic manifold of the collisional system in a diabatic electronic basis can be written as

$$H^d = T_N \begin{pmatrix} 1 & 0 \\ 0 & 1 \end{pmatrix} + \begin{pmatrix} U_{11} & U_{12} \\ U_{21} & U_{22} \end{pmatrix}, \quad (2)$$

where T_N represents the nuclear kinetic energy operator, which is diagonal in this basis. In terms of the mass-scaled body-fixed (BF) Jacobi coordinates R (the distance of the atom from the center of mass of the diatomic reagent molecule), r (the internuclear distance of the reagent molecule) and γ (the angle between \vec{R} and \vec{r}) and for total angular momentum $J \neq 0$, it is given by

$$T_N = -\frac{\hbar^2}{2\mu} \left[\frac{\partial^2}{\partial R^2} + \frac{\partial^2}{\partial r^2} \right] + \frac{\hat{j}^2}{2\mu r^2} + \frac{\hat{l}^2}{2\mu R^2}. \quad (3)$$

The quantities U_{11} and U_{22} in Eq. (2) are the energies of the two diabatic electronic states and, $U_{12} = U_{21}$, represent their coupling potential. The operator \hat{j} defines the diatomic rotational angular momentum associated with the Jacobi angle γ , and \hat{l} is the orbital angular momentum operator. The quantity, $\mu = \sqrt{\frac{m_a m_b m_c}{m_a + m_b + m_c}}$ is the three-body scaled reduced mass (calculated accordingly from the masses of the three atoms A, B and C involved in the reaction $A + BC$). The BF z -axis is defined to be parallel to \vec{R} and the diatom lies in the (x, z) plane. The quantity \hat{l}^2 is expressed as

$$\hat{l}^2 \equiv (\hat{J} - \hat{j})^2 = \hat{J}^2 + \hat{j}^2 - 2\hat{J}_z \hat{j}_z - \hat{J}_+ \hat{j}_- - \hat{J}_- \hat{j}_+, \quad (4)$$

where \hat{J} is the total angular momentum operator and \hat{j}_z and \hat{j}_\pm are the BF z -components of the respective operators. Within the CS [18] approximation the last two terms of Eq. (4) are neglected. The diabatic electronic matrix of Eq. (2) is obtained as

$$\begin{pmatrix} U_{11} & U_{12} \\ U_{21} & U_{22} \end{pmatrix} = \mathbf{S} \begin{pmatrix} V_- & 0 \\ 0 & V_+ \end{pmatrix} \mathbf{S}^\dagger \\ = \frac{V_- + V_+}{2} \mathbf{1} + \frac{V_+ - V_-}{2} \begin{pmatrix} -\cos \chi & \sin \chi \\ \sin \chi & \cos \chi \end{pmatrix}, \quad (5)$$

with

$$\mathbf{S} = \begin{pmatrix} \cos \phi & \sin \phi \\ -\sin \phi & \cos \phi \end{pmatrix}. \quad (6)$$

In Eq. (5) V_- and V_+ represents the two adiabatic PESs and, $\chi = 2\phi$, represents the pseudorotation angle related to the adiabatic-to-diabatic mixing angle ϕ in a linear coupling approximation [30]. The two adiabatic sheets of the double many body expansion (DMBE) PES [31] are used for V_- and V_+ . We note that this diabaticization scheme is based on the idea of removing the leading (divergent) derivative coupling elements of the adiabatic basis. This has been successfully tested [30] and employed for a practical application [8]. In a later study this idea is extended and generalized to less symmetric systems and a consistent comparison of the diabatic model with the computed *ab initio* data has been made [32]. The explicit coupling between V_- and V_+ considered above includes all diagonal and off-diagonal coupling terms in addition to the GP change.

The reaction probability is calculated from the expectation value of the flux operator in the basis of energy normalized reactive scattering wave function. It is evaluated in the asymptotic product channel on a dividing surface which separates the products from the reactants. The initial state-selected (i) and energy resolved reaction probability in the diabatic electronic representation is given as [33]

$$P_i^R(E) = \frac{\hbar}{\mu} \sum_{k=1}^2 \text{Im} \left[\left\langle \phi_k^d(R, r_d, \gamma, E) \left| \frac{\partial \phi_k^d(R, r_d, \gamma, E)}{\partial r} \right\rangle \right] \right]_{r=r_d}, \quad (7)$$

where, $\phi_k^d(R, r_d, \gamma, E)$ is the energy normalized wave function (k and d are the indices for the diabatic states and the dividing surface, respectively) obtained by Fourier transforming the time-evolved WP along a dividing surface in the asymptotic product channel at, $r = r_d$. The quantity on the right hand side of Eq. (7) is integrated over the entire range of R and γ to obtain the reaction probability from a given vibrational and rotational (v, j) state of the reagent diatom.

In the adiabatic representation the electronic part of the Hamiltonian is diagonal and the nonadiabatic coupling terms appear as off-diagonal elements in the nuclear part. Consequently, the flux operator in the adiabatic electronic basis also possesses off-diagonal elements. Therefore, the probability expression in the adiabatic electronic representation contains the off-diagonal electronic contributions (for further details, see Refs. [5,33]).

The cumulative reaction probability for a given initial (v, j) state is calculated by summing up the reaction probability results for different partial wave contributions as follows [34]

$$N_{vj}(E) = \sum_{\Omega=0}^j \frac{g_{\Omega}}{(2j+1)} \sum_{J \geq \Omega}^{J_{\max}} (2J+1) P_{vj}^{\Omega}(E), \quad (8)$$

the quantity g_{Ω} is the degeneracy factor; $g_{\Omega} = 1$ for $\Omega = 0$, and $g_{\Omega} = 2$ for $\Omega \neq 0$, and Ω is projection of j (and also J) on the BF z -axis.

The total reaction cross section is given by

$$\sigma_{vj}(E) = \frac{\pi}{k^2} N_{vj}(E), \quad (9)$$

where, $k = \sqrt{2\mu_R(E - \varepsilon_{vj})}/\hbar$, with ε_{vj} representing the rovibrational energy of the diatom. The initial state-selected thermal rate constant can be obtained from the total reaction cross section [35] as

$$k_{vj}(T) = \sqrt{\frac{8k_B T}{\pi \mu_R}} \frac{1}{(k_B T)^2} \int_0^{\infty} E \sigma_{vj}(E) e^{-E/k_B T} dE, \quad (10)$$

where k_B is the Boltzmann constant. Finally, the rotationally averaged thermal rate constants can be obtained by averaging over a Boltzmann distribution of such states

$$k_v(T) = \sum_j \frac{k_{vj}(T)}{Q_{\text{rot}}} (2j+1) e^{-Bj(j+1)\hbar c/k_B T}, \quad (11)$$

where B is the rotational constant of the reagent and Q_{rot} is the rotational partition function given by

$$Q_{\text{rot}} = \sum_j (2j+1) e^{-Bj(j+1)\hbar c/k_B T}. \quad (12)$$

The computational details of the reaction probabilities, cross sections and thermal rate constants are given in the Appendix A.

3. Results and discussion

In this section, we present and discuss the reaction probability, reaction cross section and thermal rate constant results obtained for the $\text{H} + \text{D}_2$ (HD) and $\text{D} + \text{H}_2$ (HD) exchange reactions. Dynamical calculations considering both the PESs explicitly and considering the repulsive lower adiabatic PES only are referred below as the coupled and uncoupled surface calculations, respectively. The reaction probabilities are calculated up to the three-body dissociation limit of ~ 4.74 eV. In the CS model inclusion of partial wave contributions up to $J = 50$ are found to be necessary to obtain converged cross section results in this energy range, both in the coupled and uncoupled surface calculations. The convergence of each calculation is checked with respect to the choice of the numerical grid parameters given in Table 1.

3.1. Reaction probabilities

The $\text{H} + \text{D}_2$ ($v = 0, j = 0$) \rightarrow HD($\sum v', \sum j'$) + D reaction probability values as a function of the total energy E are plotted in Fig. 1 for a few selected values of the total angular momentum, $J = 0, 10, 20, 30, 40$ and 50 (indicated in the panel) and for $\Omega = 0$. We note that the pattern of variation of reaction probabilities remains similar for $\Omega \neq 0$ and to save space we do not show them here. The coupled and uncoupled surface results are shown by the solid and dashed lines, respectively. It can be seen from Fig. 1 that the threshold for the reaction shifts to the higher energy with increasing J value. The difference between the coupled and uncoupled surface results cannot be seen below the energetic minimum (~ 2.74 eV) of Cls. But above this minimum, the difference becomes noticeable. As J increases the difference between the coupled and uncoupled surface results becomes negligible. It can be seen that above $J = 20$, the coupled and uncoupled surface results merge together. Oscillations in the probability curves reveal that at low energies the reaction proceeds via resonance formation which becomes more direct at higher energies.

The $\text{D} + \text{H}_2$ ($v = 0, j = 0$) \rightarrow HD($\sum v', \sum j'$) + H reaction probability values as a function of the total energy E (D, H_2 transla-

Table 1

Numerical grid parameters and properties of the initial wavefunction used in the present study.

Parameter	Value	Description
$N_R/N_r/N_z$	128/64/48	Number of grid points
$R_{\min}/R_{\max}(a_0)$	0.1/15.34	Extension of the grid along R
$r_{\min}/r_{\max}(a_0)$	0.5/8.06	Extension of the grid along r
$\Delta R/\Delta r(a_0)$	0.12/0.12	Grid spacings along R and r
$r_d(a_0)$	4.10	Location of the dividing surface in the product channel
$R_{\text{mask}}/r_{\text{mask}}(a_0)$	11.74/4.70	Starting point of the masking function
$R_0(a_0)$	10.5	Initial location of the center of the GWP in the coordinate space
$E_{\text{trans}}(\text{eV})$	2.0	Initial translational kinetic energy
$\delta(a_0)$	0.16	Initial width parameter of the GWP
$\Delta t(\text{fs})$	0.135	Length of the time step used in the WP propagation
$T(\text{fs})$	413.76	Total propagation time

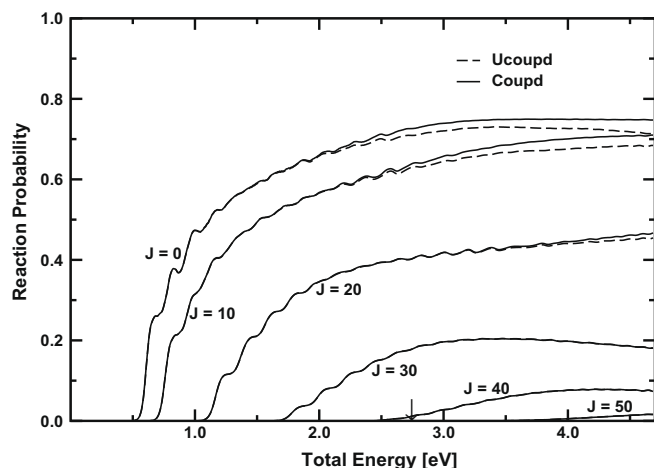


Fig. 1. Total reaction probabilities as a function of the total energy E ($\text{H} + \text{D}_2$ translational + D_2 rovibrational) for the $\text{H} + \text{D}_2(v=0, j=0) \rightarrow \text{HD}(\sum v', \sum j') + \text{D}$ exchange reaction on the DBME PES for the total angular momentum, $J=0, 10, 20, 30, 40$ and 50 (indicated in the panel) and $\Omega=0$. The coupled and uncoupled surface results are shown by the solid and dashed lines, respectively. The zero of the energy scale corresponds to infinitely separated reagents. The arrow in the abscissa indicates the location of the energetic minimum of the seam of CIs.

tional + H_2 rovibrational) are plotted in Fig. 2 for a few selected values of the total angular momentum, $J=5, 15, 25, 35$ and 45 (indicated in the panel) and for $\Omega=0$. The coupled and uncoupled surface results are shown by the solid and dashed lines, respectively. As in the case of $\text{H} + \text{D}_2$ reaction, the reaction threshold shifts to the higher energy values with increasing J due to an increase in the centrifugal barrier height. The resonance structures and their energetic locations remain same in both coupled and uncoupled surface results for a given value of J . The difference between the coupled and uncoupled surface reaction probabilities for a fixed value of J is negligible at low energies. At higher energies near and above the minimum of CIs, this difference becomes noticeable which becomes insignificant for higher J values. In this case also the dynamical event is dominated by the resonance formation at low energies and smaller J values.

We now discuss the above dynamical quantities calculated for the isotopic $\text{H} + \text{HD}$ and $\text{D} + \text{HD}$ reactions, respectively. The former gives either $\text{H}_2 + \text{D}$ (channel R1a) or $\text{HD} + \text{H}$ (channel R2a) products and the latter gives either $\text{DH} + \text{D}$ (channel R1b) and $\text{D}_2 + \text{H}$ (chan-

nel R2b) products, respectively. We in the following consider to show both the channel specific as well as total reaction probabilities. In our earlier work on the $\text{H} + \text{HD}$ system [17], a technical scaling error occurred. The H and D masses were erroneously interchanged. We have corrected the same in this work. The reaction probability values for the $\text{H} + \text{HD}$ ($v=0, j=0$) reaction as a function of the total energy E are plotted in Fig. 3a–c for five selected values of the total angular momentum, $J=0, 10, 20, 30$ and 40 and for $\Omega=0$. The reaction probabilities obtained in the uncoupled and coupled surface situations are shown by the dashed and solid lines, respectively. The reaction probabilities for channels R1a and R2a are given in panels (a) and (b), respectively, and the overall reaction probabilities (sum total of the two channel specific probabilities) are given in the panel (c). The effect of the nonadiabatic coupling on the channel specific reaction probabilities of panel (a) and (b) appears to be similar to the other isotopic variants. The opposite behavior observed between the uncoupled and coupled surface results for the channel specific probabilities shown in Fig. 5 of Ref. [17] is absent in Fig. 3a and b. Rather, the reaction probabilities for the two channels show such behavior in the latter figures for $J < 20$.

The reaction probability values for the $\text{D} + \text{HD}$ ($v=0, j=0$) reaction as a function of the total energy E are plotted in Fig. 3d–f for the $J=0, 10, 20, 30$ and 40 and for $\Omega=0$. The reaction probabilities for channels R1b and R2b are shown in panels (d) and (e), respectively. The overall reaction probabilities are given in panel (f). The coupled and uncoupled surface reaction probabilities are shown by the full and dashed lines, respectively. It can be seen that both the channel specific and the total reaction probabilities in this case exhibit similar behavior as those in case of the $\text{H} + \text{HD}$ reactions. It emerges from the above discussion that the nonadiabatic coupling have almost similar effects in the dynamics of $\text{H} + \text{H}_2$ reaction and its isotopic variants.

3.2. Initial state-selected integral reaction cross sections

The initial state-selected integral reaction cross sections as a function of collision energies for the $\text{H} + \text{D}_2$ ($v=0, j$) reaction are plotted in Fig. 4a and b for the reagent rotational states, $j=0$ and 1 , respectively. The coupled and uncoupled surface results are shown by the full and dashed lines, respectively. The cross section values for a particular j value increases reaching a maximum and then decreases. A similar trend of variation of cross sections is observed for further higher j values. The maximum cross section ($\sim 1.41 \text{ \AA}^2$) for $j=0$ occurs for the collision energy of $\sim 1.9\text{--}2.2 \text{ eV}$. The integral reaction cross sections obtained from experimental [36] and other theoretical studies [37–40] are shown in Fig. 4a and b. It can be seen from these figures that the present theoretical results are in good accord with the experiment. The difference between the cross section values calculated in the coupled and uncoupled surface situation is practically negligible. Similar conclusions have been made in a state-to-state time-dependent wave packet study of the $\text{H} + \text{D}_2$ reaction by Lu et al. employing a diabatic DMBE PES of H_3 [40] until a collision energy of 2 eV . We note that, the cross section values reported by the latter authors compare very well with ours (cf. Fig. 4a). Therefore, it appears that the “diabatic H_3 DMBE” is as “accurate” as our diabatic model for a reliable description of the reaction dynamics of $\text{H} + \text{H}_2$ and its isotopic variants. Using a line-integral approach, Xu et al. [41] apparently construct a diabatic model similar to ours and pointed out that it may yield erroneous dynamical outcomes as compared to the diabatic H_3 DMBE. This proposition is however not validated by dynamical studies and considering the present developments, it remains to be established.

The initial state-selected integral reaction cross sections for the $\text{D} + \text{H}_2$ ($v=0, j$) reaction are plotted in Fig. 4c and d for $j=0$ and 1 ,

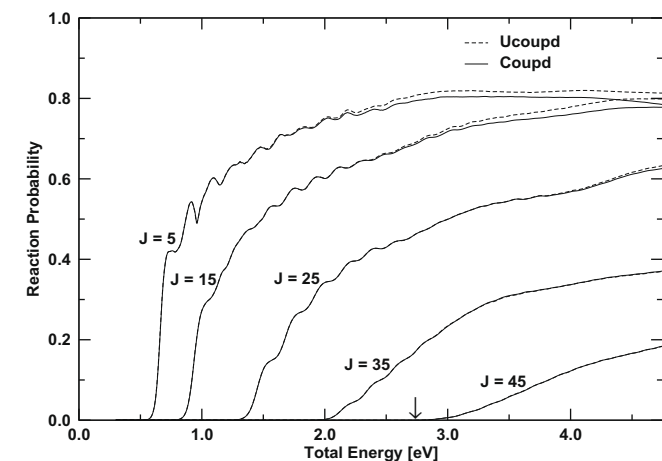


Fig. 2. Same as in Fig. 1 for $\text{D} + \text{H}_2(v=0, j=0) \rightarrow \text{HD}(\sum v', \sum j') + \text{H}$ exchange reaction for the total angular momentum, $J=5, 15, 25, 35$ and 45 (indicated in the panel) and $\Omega=0$.

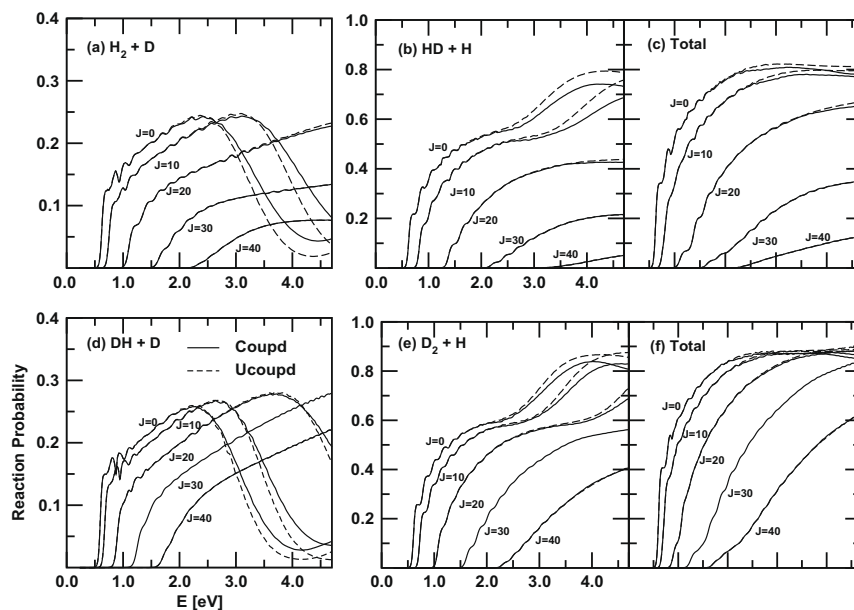


Fig. 3. Reaction probabilities of the $\text{H} + \text{HD}$ ($v = 0, j = 0$) reaction for the (a) $\text{H}_2 + \text{D}$ and (b) $\text{HD} + \text{H}$ channels as a function of total energy, E . The sum total of these probabilities are plotted in panel (c). The probabilities are shown for various values of the total angular momentum, J indicated in each panel. The coupled and uncoupled surface results are shown by the solid and dashed lines, respectively. The zero of the energy scale corresponds to infinitely separated reagents. Panel (d–f): Same as panels (a–c) but for the isotopic $\text{D} + \text{HD}$ ($v = 0, j = 0$) reaction.

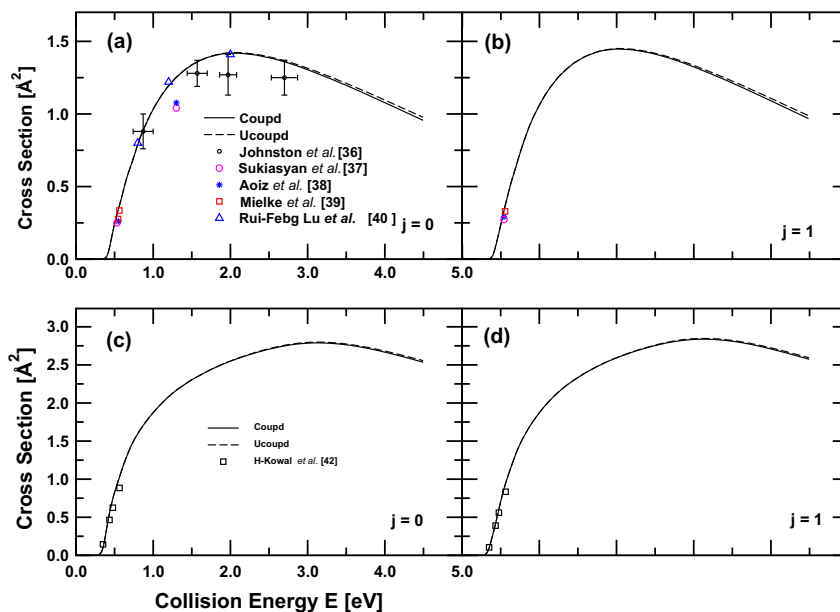


Fig. 4. Initial state-selected integral reaction cross sections of the $\text{H} + \text{D}_2$ ($v = 0, j$) (panels a and b) and $\text{D} + \text{H}_2$ ($v = 0, j$) (panels c and d) reactions, respectively, as a function of the collision energy. The reagent rotational quantum number j is indicated in each panel. The integral reaction cross section values available in the literature are shown by different symbols (Refs. [36–40,42]) as shown in the figures.

respectively. The integral reaction cross section increases, reach a maximum value ($\sim 2.78 \text{ \AA}^2$) and then decreases with increasing energy. The $\text{D} + \text{H}_2$ reaction cross sections are larger than those of $\text{H} + \text{D}_2$ reaction for a given energy. This observation is consistent with the available experimental [36] and theoretical [42] data. The larger cross section of $\text{D} + \text{H}_2$ reaction is interpreted to be due to efficient transfer of the collision energy of the heavier D atom to the vibrational degree of freedom of the lighter H_2 molecule. The difference between the uncoupled and coupled surface results is negligible in case of the $\text{D} + \text{H}_2$ reaction also. Similar variation of cross sections are obtained for further higher values of j .

The initial state-selected integral reaction cross sections for the $\text{H} + \text{HD}$ ($v = 0, j$) reaction are plotted in Fig. 5a–l as a function of the collision energy. The cross section values for the R1a and R2a channels are shown in panels (a–d) and (e–h) for $j = 0–3$, respectively. The cross section values calculated in the coupled and uncoupled surface situation are shown by the full and dashed lines, respectively. The total cross section (sum of the two channel specific cross sections) values are shown in panels (i–l) for $j = 0–3$, respectively. For any given value of j , the cross section values of the R1a channel are larger than those of the R2a channel. The skew angle of the R2a channel is much larger than the R1a channel (70.53° vs.

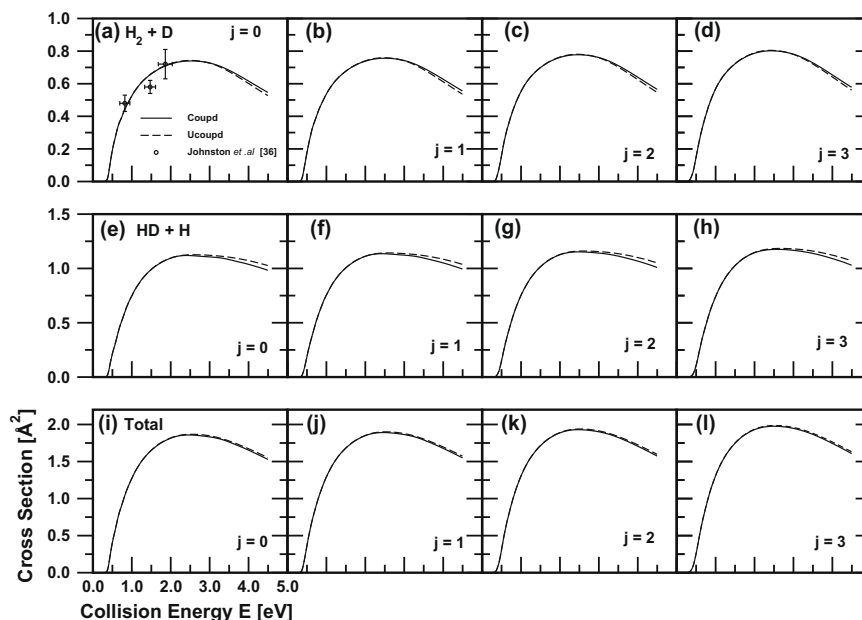


Fig. 5. Same as in Fig. 4 for the $\text{H}_2 + \text{D}$ channel (panels a–d), $\text{HD} + \text{H}$ channel (panels e–h) and the sum total of the channel specific cross sections (panels i–l) of the $\text{H} + \text{HD}$ ($v=0, j$) reaction. The reagent rotational quantum number j is given in each panel. The circles with error bars in panel (a) are experimental values from Ref. [36].

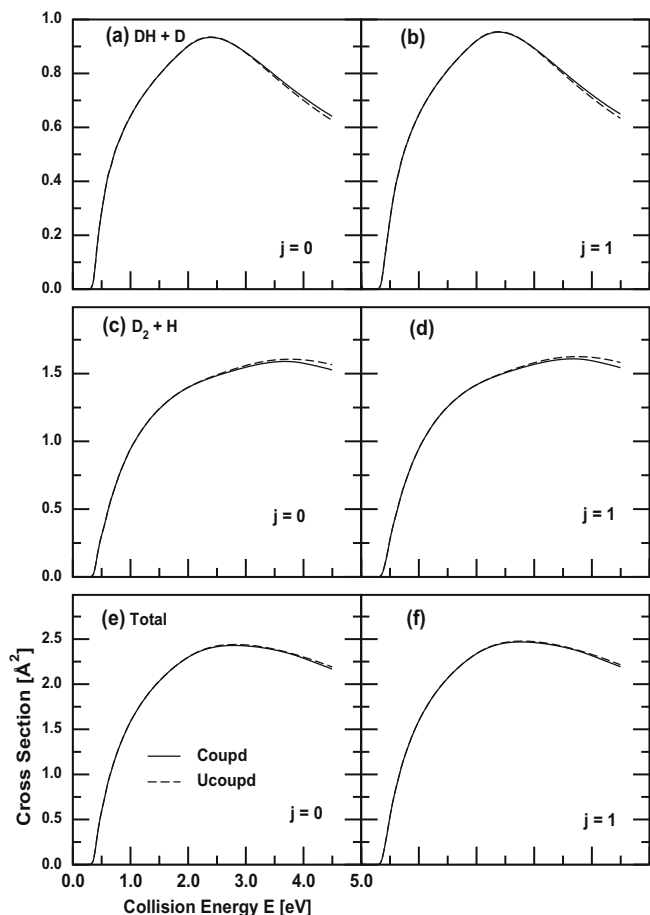


Fig. 6. Same as in Fig. 5 for $\text{D} + \text{HD}$ reaction.

54.74°). This qualitatively explains the greater reactivity of the R2a channel. The experimental data available [36] for the R1a channel for $j=0$ are also given in panel a. It can be seen that the present

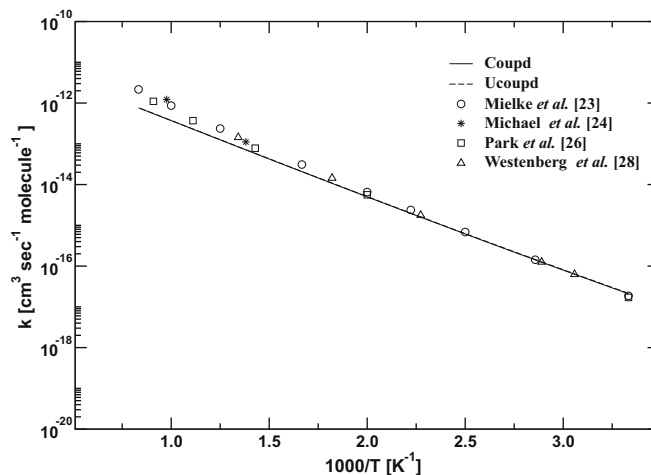


Fig. 7. Arrhenius plot of the Boltzmann averaged (over $j=0-3$ of the reagent diatom) thermal rate constants for the $\text{H} + \text{D}_2$ ($v=0$) reaction. The coupled and uncoupled surface results are shown by the solid and dashed lines, respectively. The points on the diagram represents the results from the literature [23–28].

theoretical results are fairly in good accord with the experiment. Minor difference between the cross section values calculated in the coupled and uncoupled surface situations are seen only above the minimum of the seam of CIs particularly, for the R2a channel. This difference becomes negligible in the total reaction cross sections shown in panels (i–l). We note that the above figures replace Figs. 8–10 of Ref. [17], in which a mass scaling error occurred as mentioned above. The initial state-selected integral reaction cross section values for the $\text{D} + \text{HD}$ ($v=0, j=0-1$) reaction are plotted in Fig. 6a–f as a function of the collision energy. The cross section values for the R1b and R2b channels are shown in panels (a–b) and (c–d), respectively. The cross section values for the overall reaction are shown in panels (e–f) for $j=0$ and 1, respectively. The coupled and uncoupled surface results are shown by full and dashed lines, respectively. Analogous to the $\text{H} + \text{HD}$ reaction, the cross section values increase with energy reaching a maximum and then

decrease for a given value of j . It can be seen that both the channel specific as well as the total reactivity is more in this case compared to that for the $\text{H} + \text{HD}$ reaction. This observation is in accord with the apparent rule that the heavier D atom efficiently transfers the collision energy to the HD vibration. The reactivity of the $\text{D}_2 + \text{H}$ channel is more than that of $\text{DH} + \text{D}$ channel for any given energy. In this case the skew angle of the $\text{D}_2 + \text{H}$ channel is 65.91° and much larger than that of the $\text{DH} + \text{D}$ channel of 48.19° . The effect of nonadiabatic coupling is minimal and some minor effects are seen above the minimum of the CIs.

3.3. Thermal rate constants

The thermal rate constants obtained by statistically averaging over the rotational states, $j = 0-3$, of the D_2 molecule are shown in Fig. 7 for the $\text{H} + \text{D}_2$ ($v = 0$) reaction. The coupled and uncoupled surface results are shown by the full and dashed lines, respectively.

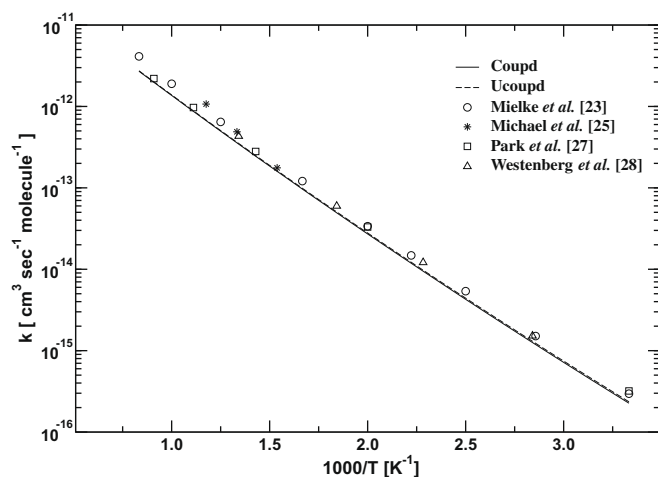


Fig. 8. Same as in Fig. 7 for the $\text{D} + \text{H}_2$ ($v = 0$) reaction.

The rate constant values available in the literature are shown by the circles (Ref. [23]), squares (Ref. [26]), triangles (Ref. [28]) and asterisks (Ref. [24]) on the diagram. The present rate constants reveal the expected Arrhenius behavior in agreement with the experimental and other theoretical data [23,26,28,24]. The observed discrepancy with the literature data mainly arises from insufficient number of j values used in the Boltzmann averaging in the present case. Furthermore, other contributing factors to this discrepancy are use of CS approximation [18] (although it is a very good approximation for the hydrogen exchange reaction) and possible inaccuracies of the underlying PESs. We note that, the main purpose of this article is to examine the effect of surface coupling on the reaction dynamics of the isotopic variants of the $\text{H} + \text{H}_2$ reaction and therefore, we limited the calculations up to $j = 3$ only. Now most importantly, Fig. 7 reveals that the difference between the coupled and uncoupled surface results is insignificant (within the drawing accuracy) in the reported temperature range of 300–1200 K.

The thermal rate constants obtained for the $\text{D} + \text{H}_2$ ($v = 0$) reaction by statistically averaging over the rotational states, $j = 0-3$, are shown in Fig. 8. The coupled and uncoupled surface results are shown by the solid and dashed lines, respectively. The rate constant values available in the literature are shown by different symbols [23,25,27,28] on the diagram. The rate constant data reveal the expected Arrhenius behavior. It can also be seen from Fig. 8 that the difference between the coupled and uncoupled surface results are insignificant in the reported temperature range of 300–1200 K.

In Fig. 9a and b, we show the thermal rate constants obtained by statistically averaging over the rotational states $j = 0-3$ for the R1a and R2a channels of the $\text{H} + \text{HD}$ reaction, respectively. The coupled and uncoupled surface results are shown by the circles and dashed lines, respectively. The rate constant values available in the literature are shown by the asterisks (Ref. [22]) and triangles (Ref. [29]) on the diagram. Also in Fig. 9a and b the thermal rate constants obtained by statistically averaging over the rotational states, $j = 0-10$, of the HD molecule for the R1a and R2a channels of the $\text{H} + \text{HD}$ reaction in the uncoupled surface situation are shown by the dots.

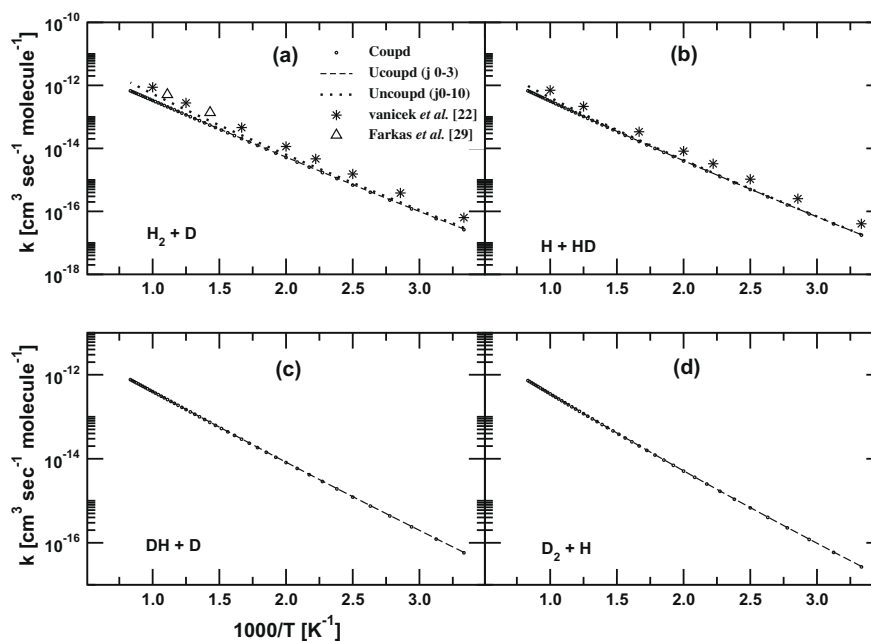


Fig. 9. Arrhenius plot of the Boltzmann average (over $j = 0-3$ (circles and dashed lines) or over $j = 0-10$ (dots) of the reagent diatom) for $\text{H}_2 + \text{D}$ and $\text{H} + \text{HD}$ reaction in panels (a) and (b), respectively. The coupled and uncoupled surface results are shown by circles and dashed lines, respectively. The asterisks and triangles represent available results from the Ref. [22] and Ref. [29] respectively. Same as above for $\text{D} + \text{HD}$ reaction shown in panels (c) and (d), respectively.

The latter results reveal better agreement with the literature data [22,29] when contributions from higher j values are included in the Boltzmann averaging. The difference between the thermal rate constants calculated in both coupled and uncoupled surface situations are again insignificant in this case. Finally we show the thermal rate constant values obtained by statistically averaging over the rotational states $j = 0-3$ for the R1b and R2b channels of the D + HD reaction in Fig. 9c and d, respectively. The rate constant data do not reveal any effects of nonadiabatic coupling in this case also.

4. Summary

A theoretical account of the electronic nonadiabatic coupling effects on the dynamics of H + D₂ (HD) and D + H₂ (HD) reactions is presented in this article. The hydrogen exchange reaction occurs on the repulsive lower adiabatic sheet of the JT split degenerate ground electronic manifold of H₃. Quantum dynamical calculations are carried out employing diabatic electronic states and a time-dependent WP method within the CS approximation and dynamical quantities viz., the initial state-selected energy resolved total reaction probabilities, integral reaction cross sections and thermal rate constants are reported. The effect of electronic nonadiabatic coupling on these observables is explicitly examined.

Like in the case of the H + H₂ reaction, the impact of nonadiabatic coupling on the above deuterated variants is found to be minor. Mild effect of surface coupling shows up only beyond the energetic minimum of the seam of conical intersections. Integral reaction cross sections are reported over a wide energy range starting from the onset of the reaction to the three-body dissociation limit. The calculated cross sections compare well with the available experimental data. The Boltzmann averaged thermal rate constants are found to be essentially same in the uncoupled and coupled surface situations for these reactions. The findings of this paper are in general agreement with the recent literature data obtained by including the GP effect only. Although not clearly understood, we reiterate that the seam of CIs in H₃ occurs at the D_{3h} configuration whereas, the minimum energy path for the reactive scattering occurs at the collinear geometry. This is perhaps one of the reasons that the surface coupling effects are minor on the dynamics of this prototypical reaction despite the minimum energy path is expected to be less relevant for the higher collision energies considered here. The exact reason, however, remains to be uncovered.

Acknowledgment

We thank the Department of Science and Technology, New Delhi, for the financial support (through Grant No. DST/SF-04/2006). The computational facilities provided under the UPE and HPCF programs of the University Grant Commission and the Department of Science and Technology, New Delhi, respectively, in CMSD of the University of Hyderabad are gratefully acknowledged. TRR also thank the Council of Scientific and Industrial Research for a junior research fellowship.

Appendix A

The wavefunction pertinent to the initial conditions of the present atom–diatom reacting system can be written as a product of the translational wavefunction $F(R)$, for which a minimum uncertainty Gaussian wave packet (GWP) is chosen for the motion along R , and the rovibrational wavefunction of ϕ_{vj} of the reagent molecule as

$$|\Psi_{\Omega}^j(R, r_m, \gamma_n, t = 0)\rangle = \sqrt{\omega_n} F(R) \phi_{vj}(r_m) \tilde{P}_j^{\Omega}(\cos \gamma_n), \quad (\text{A1})$$

where

$$F(R_l) = \left(\frac{1}{2\pi\delta^2}\right)^{\frac{1}{4}} \exp\left[-\frac{(R_l - R_0)^2}{4\delta^2} - ik_0(R_l - R_0)\right]. \quad (\text{A2})$$

Here R_l, r_m and γ_n are the grid points in the (R, r, γ) space, δ is the width parameter of GWP, R_0 and k_0 correspond to the location of its maximum in the coordinate and momentum space, respectively. We have used the sine discrete variable (sine-DVR) representation approach of Colbert and Miller [43] to solve the rovibrational eigenvalue equation for ϕ_{vj} . This wavefunction is initially located in the reagent asymptotic region of the repulsive lower adiabatic sheet V_- of the DMBE PES. It is then transformed to the diabatic electronic basis. The two components of these diabatic initial wavefunction can be written in the vector notation as

$$\Psi^d(R, r, \gamma, t = 0) = \psi_1^d(R, r, \gamma, t = 0) \begin{pmatrix} 1 \\ 0 \end{pmatrix} + \psi_2^d(R, r, \gamma, t = 0) \begin{pmatrix} 0 \\ 1 \end{pmatrix}, \quad (\text{A3})$$

where $\begin{pmatrix} 1 \\ 0 \end{pmatrix}$ and $\begin{pmatrix} 0 \\ 1 \end{pmatrix}$ indicate the first and the second diabatic electronic state with energy U_{11} and U_{22} , respectively.

The TDSE is then solved numerically in order to calculate the wave function at time t . For this purpose, the time axis is divided into N segments of length Δt and the exponential time evolution operator of Eq. (1) is then approximated by the Chebyshev polynomial expansion method [44] at each time step. The fast Fourier transformation method (FFT) [45] is used to evaluate the action of the radial kinetic energy operators on the wavefunction, whereas, the action of the angular kinetic energy operator is evaluated by a discrete variable representation (DVR) [46] method. For latter purpose we construct the γ grid by diagonalizing the $\cos \gamma$ operator in the basis of the associated Legendre polynomials. The resulting diagonal elements define the nodes of a n -point Gauss Legendre quadrature [47] and the DVR to the finite basis representation transformation matrix is given by the eigenvector matrix U . The quadrature weight associated with the grid points are calculated by $w_n^{1/2} = \sqrt{\frac{2^{K+1}K!}{(2K+1)!}} \sin^{-K}(\gamma_n) U_{1n}$, where U_{1n} refers to the first row of U (the lowest value of j , i.e., $j = \Omega$) [48]. Finally the unphysical reflections at the grid boundaries are controlled by multiplying a damping function [49]

$$f(X_i) = \sin\left[\frac{\pi}{2} \frac{(X_{\text{mask}} + \Delta X_{\text{mask}} - X_i)}{\Delta X_{\text{mask}}}\right], \quad X_i \geq X_{\text{mask}}, \quad (\text{A4})$$

to the WP at each time step. In the above equation X_{mask} is the point at which the damping function is initiated and ΔX_{mask} ($=X_{\text{max}} - X_{\text{mask}}$) is the width of X over which the function decays from 1 to 0, with X_{max} being the maximum value of X in that direction. The properties of the initial WP and the grid parameters used for the numerical calculations are listed in Table 1.

References

- [1] S.C. Althorpe, D.C. Clary, Ann. Rev. Phys. Chem. 54 (2003) 493.
- [2] H.A. Jahn, E. Teller, Proc. Roy. Soc. (London) Ser. A 161 (1937) 220.
- [3] G. Herzberg, H.C. Longuet-Higgins, Discussions Faraday Soc. 35 (1963) 77.
- [4] R.N. Porter, R.M. Stevens, M. Karplus, J. Chem. Phys. 49 (1968) 5163.
- [5] S. Mahapatra, H. Köppel, L.S. Cederbaum, J. Phys. Chem. A 105 (2001) 2321.
- [6] F. Bouakline, S.C. Althorpe, D.P. Ruiz, J. Chem. Phys. 128 (2008) 124322.
- [7] R. Bruckmeier, Ch. Wunderlich, H. Figger, Phys. Rev. Lett. 72 (1994) 2550; D. Azinovic, R. Bruckmeier, Ch. Wunderlich, H. Figger, G. Theodorakopoulos, I.D. Petsalakis, Phys. Rev. A 58 (1998) 1115.
- [8] S. Mahapatra, H. Köppel, Phys. Rev. Lett. 81 (1998) 3116; S. Mahapatra, H. Köppel, J. Chem. Phys. 109 (1998) 1721.
- [9] M. Born, R. Oppenheimer, Ann. Phys. 84 (1927) 457.
- [10] H.C. Longuet-Higgins, Proc. Roy. Soc. (London) Ser. A 344 (1975) 147.
- [11] Y.M. Wu, A. Kuppermann, B. Lepetit, Chem. Phys. Lett. 186 (1991) 319; A. Kuppermann, Y.M. Wu, Chem. Phys. Lett. 349 (2001) 537.
- [12] C.A. Mead, D.G. Truhlar, J. Chem. Phys. 70 (1979) 2284.

- [13] C.A. Mead, J. Chem. Phys. 72 (1980) 3839.
- [14] B.K. Kendrick, J. Chem. Phys. 112 (2000) 5679;
B.K. Kendrick, J. Phys. Chem. A 107 (2003) 6739;
B.K. Kendrick, J. Chem. Phys. 118 (2003) 10502.
- [15] J.C. Juanes-Marcos, S.C. Althorpe, J. Chem. Phys. 122 (2005) 204324.
- [16] J.C. Juanes-Marcos, S.C. Althorpe, E. Wrede, Science 309 (2005) 1227.
- [17] B. Jayachander Rao, R. Padmanaban, S. Mahapatra, Chem. Phys. 333 (2007) 135.
- [18] R.T. Pack, J. Chem. Phys. 60 (1974) 633;
P. McGuire, D.J. Kouri, J. Chem. Phys. 60 (1974) 2488.
- [19] S. Ghosal, B. Jayachander Rao, S. Mahapatra, J. Chem. Sci. 119 (2007) 401.
- [20] B. Jayachander Rao, S. Mahapatra, Ind. J. Phys. 81 (2007) 1003.
- [21] B. Jayachander Rao, S. Mahapatra, J. Chem. Sci. (in press).
- [22] J. Vaníček, W.H. Miller, J.F. Castillo, F.J. Aoiz, J. Chem. Phys. 123 (2005) 054108.
- [23] S.L. Mielke, K.A. Peterson, D.W. Schwenke, B.C. Garrett, D.G. Truhlar, J.V. Michael, M.-C. Su, J.W. Sutherland, Phys. Rev. Lett. 91 (2003) 063201.
- [24] J.V. Michael, J.R. Fisher, J. Phys. Chem. 94 (1990) 3318.
- [25] J.V. Michael, J. Chem. Phys. 92 (1990) 3394.
- [26] T.J. Park, J.C. Light, J. Chem. Phys. 96 (1992) 8853.
- [27] T.J. Park, J.C. Light, J. Chem. Phys. 94 (1991) 2946.
- [28] A.A. Westenberg, N. De Haas, J. Chem. Phys. 47 (1967) 1393.
- [29] A. Farkas, L. Farkas, Proc. R. Soc. London A 152 (1935) 124.
- [30] A. Thiel, H. Köppel, J. Chem. Phys. 110 (1999) 9371.
- [31] A.J.C. Varandas, F.B. Brown, C.A. Mead, D.G. Truhlar, N.C. Blais, J. Chem. Phys. 86 (1987) 6258.
- [32] H. Köppel, J. Gronki, S. Mahapatra, J. Chem. Phys. 115 (2001) 2377.
- [33] S. Mahapatra, Quantum reaction dynamics on multi-sheeted potential energy surfaces, in: W. Domcke, D.R. Yarkony, H. Köppel (Eds.), Conical Intersections: Electronic Structure Dynamics and Spectroscopy, World Scientific, Singapore, 2004, p. 555.
- [34] J.Z.H. Zhang, Theory and Application of Quantum Molecular Dynamics, World Scientific, Singapore, 1999.
- [35] F.J. Aoiz, L. Bañares, J.F. Castillo, J. Chem. Phys. 111 (1999) 4013.
- [36] G.W. Johnston, B. Katz, K. Tsukiyama, R. Bersohn, J. Phys. Chem. 91 (1987) 5445.
- [37] S. Sukiasyan, H.-D. Meyer, J. Phys. Chem. A 105 (2001) 2604.
- [38] F.J. Aoiz, L. Bañares, V. J. Herrero, V.S. Rábanos, I. Tanarro, J. Phys. Chem. A 101 (1997) 6165.
- [39] S.L. Mielke, D.G. Truhlar, J. Phys. Chem. 98 (1994) 1053.
- [40] Rui-Feng Lu, Tian-Shu Chu, Yan Zhang, Ke-Li Han, A.J.C. Varandas, John Z.H. Zhang, J. Chem. Phys. 125 (2006) 133108.
- [41] Z. Xu, M. Baer, A.J.C. Varandas, J. Chem. Phys. 112 (2000) 2746.
- [42] S. Hochman-Kowal, A. Persky, Chem. Phys. 222 (1997) 29.
- [43] D.T. Colbert, W.H. Miller, J. Chem. Phys. 96 (1992) 1982.
- [44] H. Tal-Ezer, R. Kosloff, J. Chem. Phys. 81 (1984) 3967.
- [45] D. Kosloff, R. Kosloff, J. Comput. Phys. 52 (1983) 35.
- [46] J.C. Light, I.P. Hamilton, J.V. Lill, J. Chem. Phys. 82 (1985) 1400;
Z. Bačić, J.C. Light, Ann. Rev. Phys. Chem. 40 (1989) 469.
- [47] W.H. Press, B.P. Flannery, S.A. Teukolsky, W.T. Vetterling, Numerical Recipes in Fortran: The Art of Scientific Computing, 2nd ed., Cambridge University Press, New York, 1986.
- [48] M.H. Beck, A. Jäckle, G.A. Worth, H.-D. Meyer, Phys. Rep. 324 (2000) 1.
- [49] S. Mahapatra, N. Sathyamurthy, J. Chem. Soc. Faraday Trans. 93 (1997) 773.